Highly Efficient Photothermal Effect by Atomic-Thickness Confinement in Two-Dimensional ZrNCl Nanosheets

Feng Feng,[†] Hongyan Guo,[†] Dianqi Li,[†] Changzheng Wu,[*,†] Junchi Wu,[†] Wenshuai Zhang,[‡] Shaojuan Fan,[‡] Yuchen Yang,[§] Xiaojun Wu,[†] Jinlong Yang,[†] Bangjiao Ye,[‡] and Yi Xie[†]

[†]Hefei National Laboratory for Physical Sciences at Microscale & Collaborative Innovation Center of Chemistry for Energy Materials, University of Science & Technology of China, Hefei, Anhui 230026, P.R. China, [‡]Department of Modern Physics & State Key Laboratory of Particle Detection and Electronics, University of Science & Technology of China, Hefei, Anhui 230026, P.R. China, and [§]Department of Physics and Astronomy, University of Utah, Salt Lake City, Utah 84112, United States

ABSTRACT We report a giant photothermal effect arising from quantum confinement in two-dimensional nanomaterials. ZrNCl ultrathin nanosheets with less than four monolayers of graphene-like nanomaterial successfully generated synergetic effects of larger relaxation energy of photon-generated electrons and intensified vibration of surface bonds, offering predominantly an enhancement of the electron–phonon interaction to a maximized extent. As a result, they could generate heat flow reaching an ultrahigh value of 5.25 W/g under UV illumination with conversion efficiency up to 72%. We anticipate that enhanced electron–phonon coupling in a quantum confinement system will be a powerful tool for optimizing photothermal conversion of inorganic semiconductors.

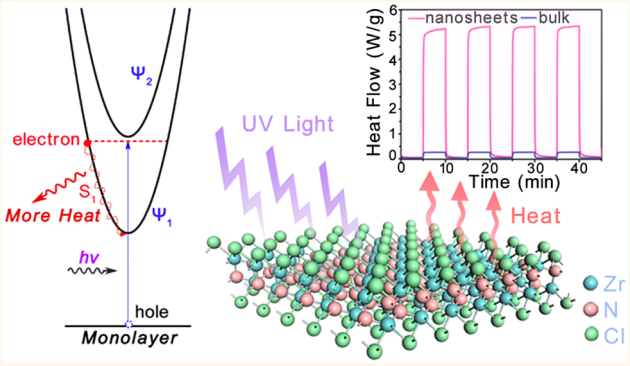

KEYWORDS: photothermal effect · quantum confinement · electron–phonon interaction · ultrathin nanosheets · energy conversion

Energy transformation from photon energy on the edge of the visible regime has greatly affected life processes, such as catalysis, detection, imaging, *etc.*, which leads to tremendous conveniences for modern life in the past century.[1−4] In this regard, every category of energy conversion from ultraviolet (UV) light has indeed brought a revolutionary impact on the scientific area and its intriguing applications. For example, electrical energy converted from UV light finds useful applications in photovoltaic devices and photodetectors;[5−7] chemical energy converted from UV light accelerates chemical reactions in the photocatalysis process.[8,9] For photon to thermal energy conversion, as is well-known, infrared (IR) light is capable of photothermal conversion through an infrared–phonon coupling effect, but with weaker photon energy;[10] However, UV light with stronger photon energy matches the transition energy between valence and conduction bands of semiconductors to excite electrons,[11] not to effectively trigger photothermal conversion. Recent studies have made great efforts in photothermal conversion in order to utilize the whole solar photon spectrum;[12,13] however, the exact working mechanism of conversion from UV light to thermal energy is still unclear and lacks an effective way to optimize their conversion efficiencies from this stronger photon energy form. Therefore, building a bridge between UV photon energy and harvesting heat not only is a long-standing scientific issue to be conquered but also holds great promise for providing a new cold-light-driven heating source as well as improving solar thermal utilizations.[14] Electron–phonon coupling in the UV excitation system shows promise for solving the problem of energy conversion from UV light to thermal energy, where photogenerated electrons inevitably interact with phonons, leading to energy relaxation in the form of heat release.[15] Thus, enhancing

* Address correspondence to czwu@ustc.edu.cn.

Received for review November 10, 2014 and accepted January 16, 2015.

Published online January 16, 2015
10.1021/nn506473m

electron−phonon interaction to a maximized extent represents a great opportunity for achieving giant photothermal effects. Here, we demonstrate that the quantum confinement effect in two-dimensional (2D) nanomaterials maximizes the enhancement of electron−phonon interactions, successfully realizing a giant photothermal effect in semiconducting materials.

Interest in ultrathin 2D nanomaterials, especially inorganic graphene-like materials, has surged since the discovery of graphene, due to their abundant elemental composition, special crystallographic structure, and diversified electronic properties.[16−18] The unique electron and phonon structures of 2D nanomaterials create an intensive electron−phonon interaction, providing a unique platform to investigate the conversion from photons to heat. Strong confinement effect in one or a few atom thick 2D nanomaterial enables a tunable energy band gap and thus simplifies band structure.[19] In 2D ultrathin nanosheets, photoexcited electrons can be roughly modeled as 2D free electron gas confined in a one-dimensional (1D) potential well,[20] in which the energy state can be defined as

$$E_n = n^2h^2/(8ma^2) + k^2h^2/(8m\pi^2) \quad (1)$$

where n is and integer that describes the quantum number in a confined direction; k is the wavenumber in the two-dimensional plane; h is Planck's constant; m is the effective mass of the electron; and a is the thickness of the layered material. As demonstrated in Figure 1a, to remain more energetically stable in a specific excited state, a photon-excited electron, whose initial wavenumber is k_0 at the nth state, will reach the lowest energy point ($k = 0$) by releasing relaxation energy (ΔE)

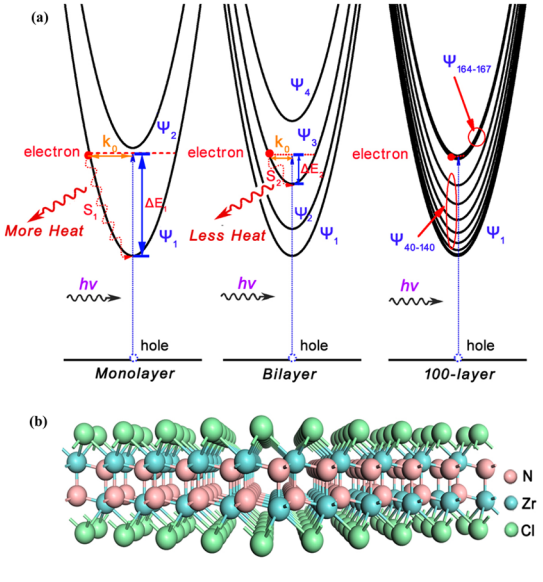

Figure 1. (a) Schematic illustration of excited electron relaxation process in a 2D nanostructure with an increased number of layers (left to right: monolayer, bilayer, and 100 layers). (b) Crystallographic structure of monolayer ZrNCl.

to thermal energy without radiation by electron−phonon interaction. According to eq 1 and calculations, a larger of thickness value (a) of the material corresponds to denser excited states, which means electrons in the monolayer can jump to a lower excited state, but with a k_0 value higher than that in the bilayer when excited by the same photon. In the bulk structure, with significantly increased 100 layers, the initial wavenumber k_0 becomes extremely small. Hence, reducing the thickness in the layered materials will generally increase the initial wavenumber k_0 of an excited electron and, consequently, create a stronger electron−phonon interaction, which will be favorable for transformation into greater thermal energy. Moreover, due to the elimination of interlayer van der Waals force and plenty of exposed surface atoms,[21−23] surface bond vibrations would be much freer in 2D nanomaterials. Therefore, the confinement effect in 2D nanomaterials creates the synergetic effect of increased relaxation energy as well as surface bond vibration, which shows advances for enhancing the electron−phonon interaction to trigger photothermal effects.

Structural analysis inspires us that lamellar zirconium nitride chloride (ZrNCl), with unique four-layer atoms in a monolayer, shows promise in creating a strong confinement effect and thus enhancing electron−phonon interactions. The unit cell of SmSI-type β-ZrNCl consists of triple layers of [Cl−Zr−N−Cl] atom stacking. The weak van der Waals interaction between adjacent layers of ZrNCl enables a nanosheet structure with the height down to four atomic layers thick. Furthermore, in each [Cl−Zr−N−Cl] layer, a double honeycomb-like ZrN structure is sandwiched between two layers of Cl atoms (Figure 1b), featuring two sets of relatively independent Zr−Cl bonds,[24] which would provide extra vibrations for better electron−phonon coupling. With the quantum confinement effect in a unique atomic structure, ZrNCl could be a hopeful candidate for achieving effective photo-to-thermal conversion.

Herein, we highlight a greatly enhanced electron−phonon interaction in two-dimensional nanomaterials as a new effective route to realize giant photothermal effects. With the quantum confinement effect in unique atomic structure, ZrNCl ultrathin nanosheets with less than four monolayers, as a new 2D graphene-like material, generates heat flow with an ultrahigh value of 5.25 W/g under UV irradiation at a high conversion efficiency of 72%, which is dozens of times higher compared with other wide-gap semiconductors, recording the best value of direct UV photothermal effect among inorganic materials nowadays. This study not only opens up a new direction to find a promising candidate for giant photothermal effects in semiconducting solids but also realizes a new effective energy conversion form of UV light.

RESULTS AND DISCUSSION

Synthesis and Characterization. In the typical process (Materials and Methods), ZrNCl ultrathin nanosheets were chemically exfoliated for the first time by ultrasonication of bulk precursor Li-intercalated ZrNCl. Systematic characterizations have been used to verify the few-atom-layer structure and composition of ZrNCl ultrathin nanosheets. The X-ray diffraction (XRD) pattern of exfoliated ZrNCl nanosheets showed a high *c*-orientation feature, and only (00*n*) peaks have been detected (top of Figure 2a), indicating a high-quality ZrNCl structure. XPS indicated elemental valence and compositions of ZrNCl ultrathin nanosheets. Supporting Information Figure S1 showed that Zr $3d_{5/2}$ and Zr $3d_{3/2}$ peaks from both bulk and nanosheet samples were located at 182.1 and 184.5 eV with a spin−orbital splitting energy at 2.4 eV. The ratio of peak intensity between these two peaks was close to 3:2. These peak features were consistent with reported Zr^{4+} signals in X-ray photoelectron spectra (XPS),[25] which verified that no chemical impurities were brought into the system under ultrasonic exfoliation. The quantification of Zr, N, and Cl peaks in the XPS spectra further confirmed that the elemental ratio of Zr/N/Cl was close to 1:1:1. Furthermore, elemental mapping images (Figure S02) also confirmed that Zr, N, and Cl were distributed homogeneously in the final nanosheet products without any contaminated elements. The structure and composition characterization described above indicated that our final product maintained stable chemical stoichiometric properties with a unique 2D structure.

Microstructural characterizations were taken to reveal the morphology and crystalline structure of ZrNCl nanosheets. The SEM image showed that the bulk sample had tightly stacking layers (Figure S3), while the as-exfoliated samples were ultrathin nanosheets with lateral sizes ranging from hundreds of nanometers to about 1 μm (Figure S4). The TEM image of the exfoliated ZrNCl nanosheet in Figure 2b unraveled a freestanding, sheet-like morphology with lateral size of about 500 nm. The almost transparent feature implied the ultrathin structure of exfoliated nanosheets. AFM scanning under tapping mode was used to measure the thickness of as-obtained nanosheets. The measured height was about 3.426 and 3.944 nm (Figure 3a), corresponding to 3−4 layers, because the interplane spacing of (003) was 9.213 Å. The HRTEM image also showed the cross section of ZrNCl nanosheets, from which we measured the interplane spacing to be about 0.98 nm, close to the *d* value of the (003) plane. Furthermore, there were three to four bright and dark lattice fringes, indicating that nanosheets were stacked up by three or four ZrNCl monolayers, which agreed with the measurement

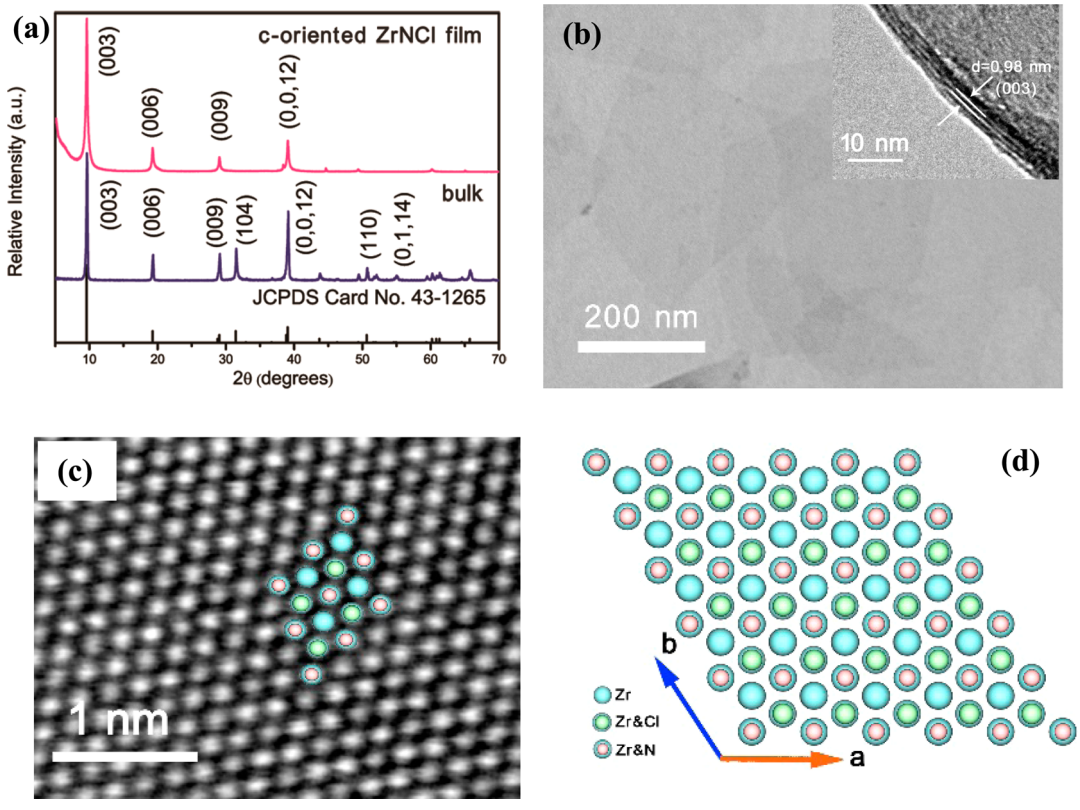

Figure 2. (a) XRD pattern of as-synthesized ZrNCl bulk sample, assembled film of ZrNCl nanosheets, and the standard XRD pattern. (b) TEM image of ultrathin ZrNCl nanosheets with a cross section image (top inset). (c) HAADF-STEM image of as-exfoliated nanosheets. (d) Schematic diagram of ZrNCl crystal structure projected along the [001] direction.

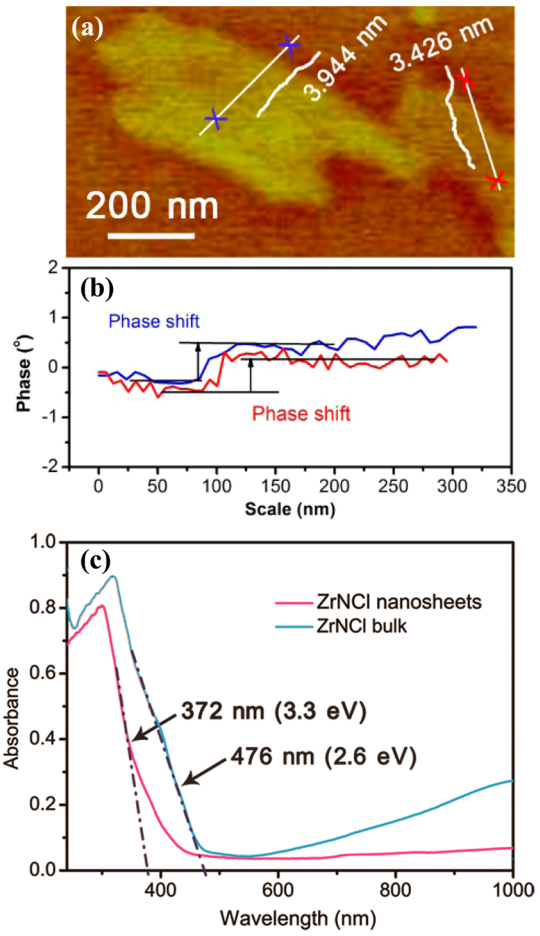

Figure 3. (a) Scanning conductance microscopy (SCM) image of ZrNCl nanosheets with the interleave mode of AFM (height was measured under tapping mode of AFM). (b) Line scan of ZrNCl nanosheets along the direction indicated by the white line in the SCM image (red line and blue line correspond to the white line with red crosses and blue crosses, respectively). (c) UV−vis absorption spectra of ZrNCl nanosheets and its bulk counterpart.

result of AFM images. High-angle annular dark-field scanning transmission electron microscopy (HAADF-STEM) image (Figure 2c) directly unveiled the single-crystalline nature and hexagonal atomic arrangement of ZrNCl nanosheets, which was consistent with the schematic diagram of the ZrNCl crystal structure viewed down the [001] zone axis (Figure 2d). All of these characterizations elucidated that ZrNCl ultrathin nanosheets with less than four [Cl−Zr−N−Cl] layers were successfully produced with high *c*-orientation and good crystallinity.

The electronic structure of ZrNCl nanosheets was investigated by combined analysis of scanning conductance microscopy (SCM) and UV−vis absorption spectroscopy. SCM (Figure 3a) inspected microscopic conductance of as-exfoliated ZrNCl nanosheets with the interleave mode of AFM *via* a dual-pass technique.[26] During the measuring process, a 5 V dc voltage was applied to the tip, and the cantilever was driven at its free resonant frequency. In the scan results (Figure 3b) from the line profile of the SCM image, ZrNCl nanosheets showed a positive phase shift with respect to the bare SiO_2 substrate, which demonstrated their semiconducting characteristics with a wide energy band gap from a microscopic viewpoint.[27] UV−vis spectra revealed that the ~2.6 eV band gap of bulk ZrNCl increased to ~3.3 eV for ZrNCl nanosheets, showing a blue shift when the thickness was down to atomic scale. Both results of the SCM image and UV−vis spectra proved that ZrNCl ultrathin nanosheets were able to absorb UV photons effectively.

As evidenced by the above characterizations, bulk ZrNCl has been successfully treated on nanosheet structures with a thickness down to the few nanometer scale, while still maintaining the polymorphic structure and elemental composition of the bulk, providing an ideal 2D nanomaterial platform to investigate the quantum confinement effect. In 2D nanomaterials, electrons excited by photons are confined in a 1D quantum well, in which energy levels are quantized and can be defined in eq 1. According to the 1D box model, as illustrated in Figure 1a, the reduction of thickness (*a*) enhances the relaxation energy of excited electrons, which enhances the probability for electron−phonon coupling. Moreover, ultrathin ZrNCl nanosheets with a special four-atom stacking structure in each layer and large exposed surface area would generate intensive vibrational modes in the 2D confined system. Therefore, with both advantages of larger relaxation energy and intense bond vibration, stronger electron−phonon coupling in ultrathin ZrNCl nanosheets could be achieved. Furthermore, ZrNCl nanosheets have strong UV absorption and weak photon luminescence (Figure S5), promising large thermal response under UV excitation.

Photothermal Effect. Heat flow released from ZrNCl nanosheets under UV illumination was detected by photo-differential scanning calorimetry (photo-DSC) (see Materials and Methods) with UV light having a wavelength of 365 nm at an intensity of 200 mW/cm^2. In this thermoanalytical technique, the heat change of a sample is characterized with/without optical illumination in isothermal mode. When the source of UV photons was on, an exothermal process was observed (Figure 4a), during which the heat flow reached 5.25 W/g, achieving energy conversion efficiency as high as 72% (Supporting Information section S7). Good photocorrosion resistance to UV light on ZrNCl nanosheets is shown in Figure S7, in which a stable and reproducible heat flow was shown within 200 min without obvious heat flow degradation. In a response and reset process, the time for reaching stable heat flow of ZrNCl nanosheets after UV light on/off was 18.6 s (response time) and 15.0 s (reset time), respectively (Figure 4b). Compared to the bulk sample, the response and reset time of bulk ZrNCl was 29.6 and 35.4 s, each of which was about twice as long as that of nanosheets, revealing a

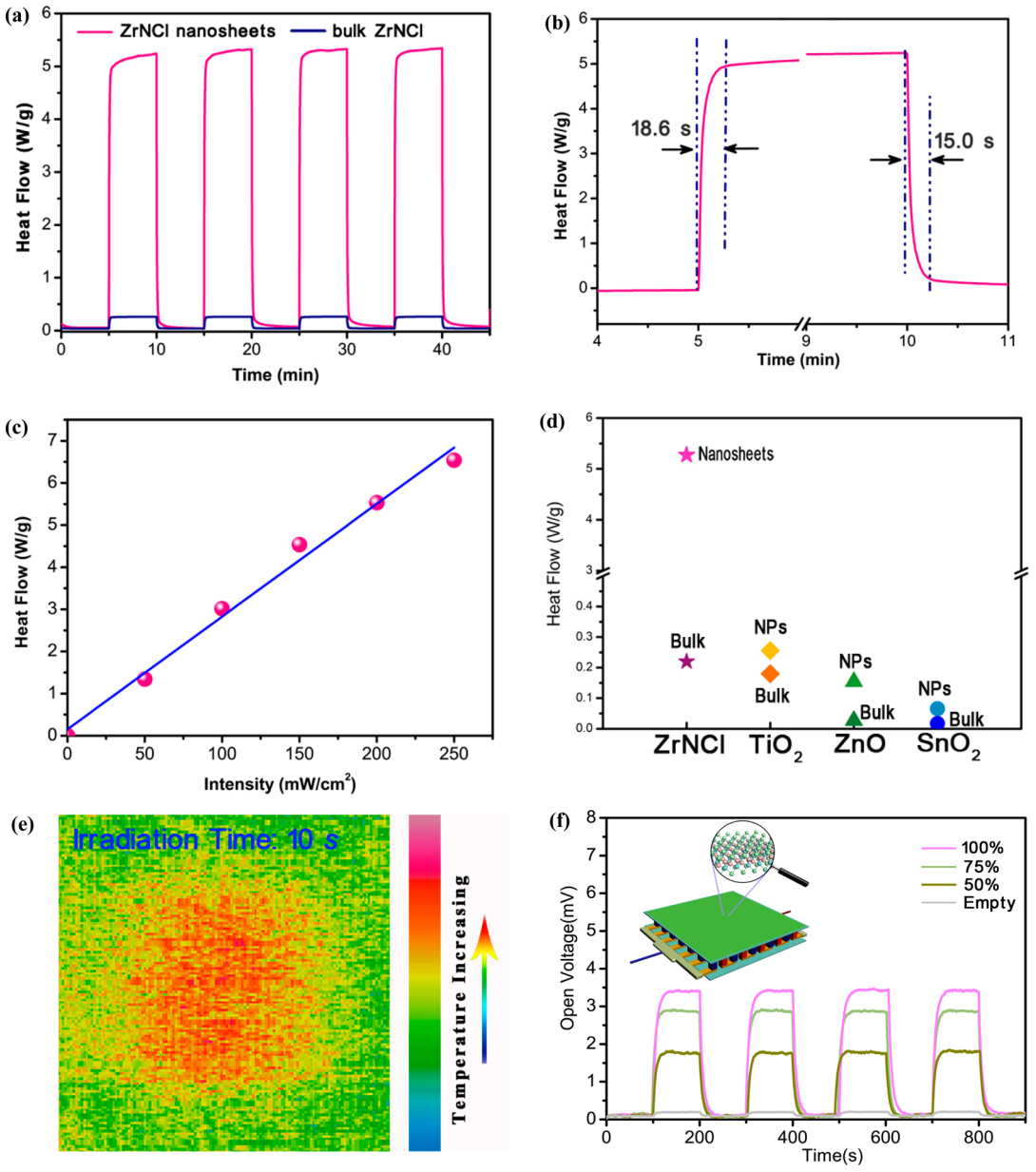

Figure 4. (a) Time-dependent photothermal response of ZrNCl nanosheets and the bulk counterpart with UV light on and off. (b) Enlarged part of one response and reset process. (c) Maximum heat flow of ZrNCl nanosheets evolved with increasing light intensity. (d) Maximum heat flow of ZrNCl nanosheets and its bulk, TiO_2, ZnO, and SnO_2 nanocrystals, and their bulk materials. (e) IR thermal image of an assembled square thin film of ZrNCl nanosheets with UV light on. (f) Time-dependent open voltage of a thermoelectric generator in which the hot junction is covered by a different area of the ZrNCl film assembled by nanosheets.

thermal diffusion time of the bulk sample that is longer than that of nanosheets (Figure S8). Considering that heat flow generated from ultrathin ZrNCl nanosheets was 24 times larger than that from the bulk sample, it was understandable that the thermal diffusion rate was not the decisive factor for the great discrepancy of heat flow. Therefore, atomic-thickness confinement in a unique four-atom ZrNCl structure of [Cl−Zr−N−Cl] in a monolayer structure, with synergic advantages of larger relaxation energy and strengthened bond vibration, enhanced the photothermal effect in ultrathin ZrNCl nanosheets. In addition, this highly efficient photo-to-thermal conversion from ZrNCl nanosheets could only be achieved by UV illumination due to energy match between UV photons and energy band gap. A green laser source of 532 nm was used to irradiate ZrNCl nanosheets as a comparison (Figure S9), from which only very little heat (0.01 W/g) was released because electrons could not be excited effectively by green light with weaker photon energy. Moreover, a linear relationship between the light intensity and the corresponding stable heat flow was observed (Figure 4c), demonstrating that the UV photothermal effect in ZrNCl nanosheets was intrinsic. The thermal response

of ZrNCl nanosheets was ultrahigh, which was confirmed by the comparison experiments of wide band gap semiconductors, such as TiO_2, ZnO, and SnO_2 nanocrystals and nanosheets (Figure S10 and Table S1). The heat flow generated from ZnO, TiO_2, and SnO_2 nanocrystals under 200 mW/cm^2 UV light (365 nm) was 0.16, 0.26, and 0.07 W/g, respectively (Figure 4d). In the same experimental condition, the converted heat flow was 0.35 W/g for ZnO nanosheets, 0.36 W/g for TiO_2 nanosheets, and 0.66 W/g for SnO_2 nanosheets. Hence, heat converted from photons by ZrNCl nanosheets was dozens of times of higher compared with that of other wide-gap semiconductors, showing the outstanding photothermal performance of ultrathin ZrNCl nanosheets.

The giant heat release in ZrNCl nanosheets was also proven by auxiliary characterization techniques of a thermal imager. A rapid infrared thermal imager visually recorded the increasing temperature caused by heat released from ZrNCl ultrathin nanosheets under UV illumination. In our experiment, ZrNCl nanosheets have been assembled into a square film *via* vacuum filtration and have been transferred onto a quartz substrate (Figure S11a). Before the UV source was turned on, the film and the substrate were in the same green color, showing that they were the same temperature (Figure S11b). After being exposed under UV photons for just 10 s, the color of the square area in the middle changed to red (Figure 4e), showing that the temperature obviously increased. The shape of the color-changed area was identical to that of the ZrNCl film, which gave solid evidence that the temperature increment resulted from the UV photothermal effect of ZrNCl nanosheets. To demonstrate practical applications, we further transferred ZrNCl thin film onto the hot junction of a commercial thermoelectric generator. When heat was released from ZrNCl nanosheets under UV illumination, temperature difference would be occur between two junctions to generate electricity. An open voltage of the generator with the UV source on/off has been measured. The wavelength of the UV source was 380 nm with an intensity of 150 mW/cm^2. The open voltage increased as the area of the covered ZrNCl thin film changed from 0 to 100% (Figure 4f). When the surface of the hot junction was completely covered by the ZrNCl film, the open voltage reached a stable value of about 3.4 mV under UV light, indicating a large temperature gradient formed between two sides of the generator, which demonstrated the exothermic heat converted from photons. The open voltage with UV light on/off was reproducible and stable, which was consistent with the cycling stability performed in the photo-DSC measurement. Moreover, an inverted-U-type relationship has been found between the thickness of the ZrNCl thin film and the open voltage of the thermoelectric generator (Figure S12). Based on above measurement, ultrathin ZrNCl nanosheets can also be used as a stable UV-driven planar heat source with higher energy conversion rate and efficiency.

UV-Raman Study. Ultrathin ZrNCl nanosheets with atomic-thickness confinement successfully accomplished the giant photothermal effect during the photon excitation process due to enhanced photoexcited electron−phonon coupling. Different types of phonons with different polarization included complexity in the electron−phonon coupling process. Under this situation, UV-Raman provided auxiliary evidence to unveil the enhanced interaction between optical phonons and photoexcited electrons in ZrNCl nanosheets. When UV photons interacted with species having a strong UV absorption, some Raman bands showed strong resonance enhancement due to the coupling between excited electrons and some phonon states.[28] In this regard, the Raman spectrum under excitation of a 325 nm laser was observed to change the vibration modes due to an enhanced electron−phonon interaction, and a 514 nm visible laser was used for comparison purposes. The Raman spectrum of ZrNCl nanosheets excited by a 514 nm laser showed almost the same feature as that of the bulk counterpart, and it is consistent with the Raman spectrum reported in previous literature,[29] which also verified the structure of ZrNCl. However, when using a 325 nm laser as an excitation source, the Raman spectrum changed greatly. As shown in Figure 5a, peak A corresponds to the out-of-plane vibration mode A_{1g} (along the *c*-axis), while peak B is associated with the in-plane vibration mode E_g (vertical to the *c*-axis).[29] Therefore, comparing the relative intensity of peaks A and B could indicate the enhancement of vibration in the corresponding direction. In this case, the intensity of peak A was much weaker than that of peak B in spectra obtained under a 514 nm laser, but the intensity of peak A was larger than that of peak B when under 325 nm laser illumination. Moreover, by comparing the ratio of peaks A and B for bulk (1.18) and nanosheet (1.31), respectively, we see that the vibration mode of A_{1g} was more enhanced when the thickness of bulk ZrNCl was down to atomic scale, which indicated a stronger electron−photon coupling. Therefore, these results proved that the vibration of the A_{1g} mode was strengthened more compared to the E_g mode under UV light illumination. This selectively enhanced Raman mode indicated that coupling between optical phonons and excited electrons occurred in the ZrNCl nanosheet structure under UV light. Additionally, in the UV-Raman spectra, a red shift of the A_{1g} mode from 586.1 to 582.2 cm^{-1} was observed between bulk and 2D ZrNCl samples, while no shift was observed for the E_g mode between the two. This energy reduction effect means that less energy was needed in the bond vibration of the A_{1g} mode, due to the elimination of van der Waals force and a more

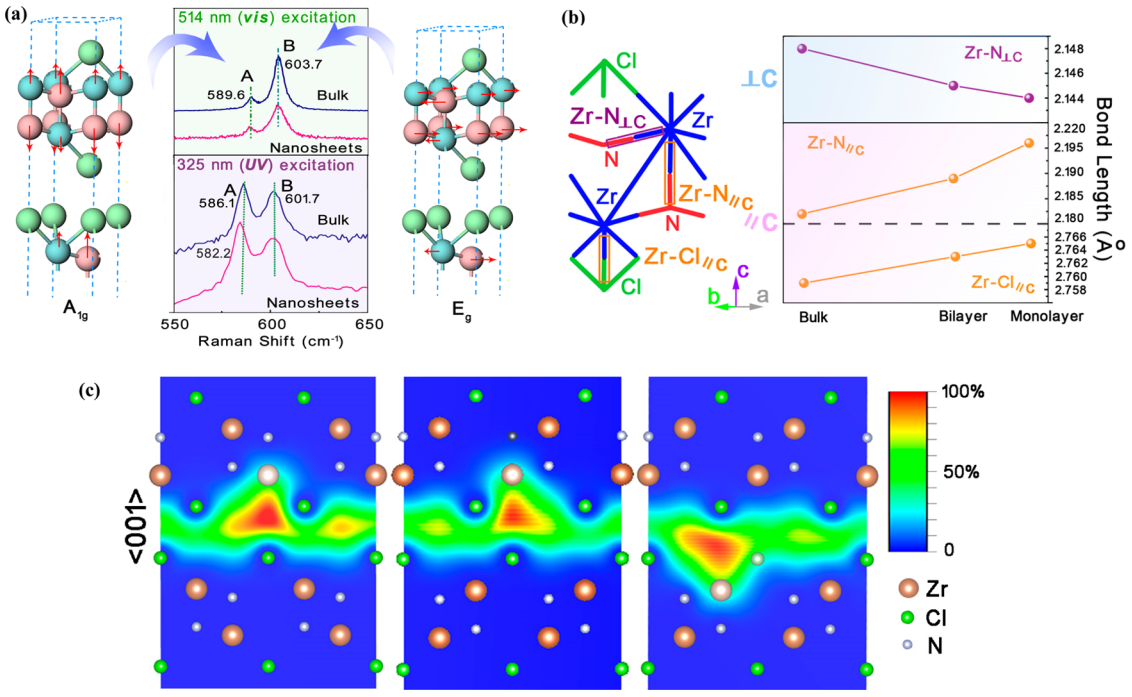

Figure 5. (a) Raman spectra of ZrNCl nanosheets and its bulk counterpart in the region of 550−650 cm^{-1} excited by 514 nm (top) and 325 nm (bottom). The left and right are A_{1g} and E_g vibration modes corresponding to A and B peaks in the Raman spectra. (b) Bond length of Zr−N (perpendicular to the *c*-axis), Zr−N (parallel to the *c*-axis), and Zr−Cl (parallel to the *c*-axis) evolved with the number of layers in the ZrNCl structure. (c) Schematic representations of trapped positrons of V_{Zr}'''', $V_{Zr}''''V_N^{\cdot\cdot}$, $V_{Zr}''''V_{Cl}^{\cdot}$ vacancy associates according to positron annihilation data.

exposed surface area in 2D ZrNCl, which would also be conducive to elevate electron−phonon interaction in ZrNCl ultrathin nanosheets.

The above UV-Raman results were further verified by a structural optimization process. Perdew−Burke−Ernzerhof functional calculation (Supporting Information section S2) was performed to uncover the microstructural evolution as a function of number of layers, in which the bond lengths of Zr−N (perpendicular to the *c*-axis), Zr−N (parallel to the *c*-axis), and Zr−Cl (parallel to the *c*-axis) bonds in bulk, bilayer, and monolayer of ZrNCl have been calculated, respectively. The evolution of each bond length is shown in Figure 5b, from which we could see that the Zr−N and Zr−Cl bonds along the *c*-axis became longer as the number of layers decreased, while the Zr−N bond perpendicular to the *c*-axis shortened a little when the number of layers decreased. The stretch of in-plane bonds facilitated the vibration modes along the *c*-axis in ZrNCl nanosheets to enhance electron−phonon interaction, which led to increased intensity and red shift of the A_{1g} mode in the UV-Raman spectrum. The calculation results brought a further insight into UV-Raman spectra, confirming the enhancement of the electron−phonon interaction along the *c*-axis in ZrNCl ultrathin nanosheets, where the quantum confinement effect was responsible for giant heat release.

Vacancy Detection. In a system under photon excitation, the sources of heat generation are not only from the electron−phonon interaction but also from the recombination process of electron−hole pairs at defects.[30] In order to study the defect conditions between ZrNCl bulk and nanosheets, we used positron annihilation and electron paramagnetic resonance (EPR) to investigate cation and anion defects, respectively. As an accurate methodology to study cation defects in materials, positron annihilation could uncover information on defects such as type and relative concentration by measuring the lifetime of positrons.[31] The lifetime spectra of ZrNCl nanosheets and its counterpart have been recorded (Figure S13), which were similar to each other and could be analyzed into two lifetime components. The components with longer lifetime (bulk = 1.044 ns and nanosheets = 1.311 ns) were ascribed to large defect clusters and interface.[32] The shorter lifetime components of the bulk and nanosheets was very close to each other (bulk = 0.292 ns and nanosheets = 0.305 ns) with very similar intensity (bulk = 97.1% and nanosheets = 95.7%), which indicated that the exfoliation process did not bring extra cation defects into the sample (Table S2). According to the theoretical calculation (Supporting Information section S2), three types of theoretical positron lifetimes were 316, 317, and 361 ps (Table S3), corresponding to three different defects where the distribution of positron annihilation was trapped, that is, Zr vacancy (V_{Zr}''''), Zr−N vacancy ($V_{Zr}''''V_N^{\cdot\cdot}$), and Zr−Cl vacancy ($V_{Zr}''''V_{Cl}^{\cdot}$), respectively (Figure 5c). Therefore, the predominant defects in both bulk and nanosheets could be assigned to V_{Zr}'''' or $V_{Zr}''''V_N^{\cdot\cdot}$. The EPR spectra of ZrNCl ultrathin

nanosheets and the bulk are shown in Figure S14, from which we could see that no obvious signal of single electron has been detected. Since anion vacancy in the ZrNCl structure would definitely leave single electrons, the EPR spectrum confirmed that no anion defects existed in the ultrathin ZrNCl nanosheets. In a word, there was no obvious discrepancy of cation and anion defects between ultrathin ZrNCl nanosheets and its bulk counterpart, which showed that defects did not have the capability of producing significant improvements in UV photothermal effect from bulk to ultrathin nanosheets, giving auxiliary evidence that the quantum confinement effect in 2D nanomaterials played a vital role in achieving giant UV photothermal effect.

CONCLUSION

In conclusion, atomic-thickness confinement in a unique ZrNCl structure of four-atom [Cl−Zr−N−Cl] in one monolayer, as a new graphene-like structure, produces synergic advantages of larger relaxation energy and strengthened bond vibration, which inevitably induced enhanced electron−phonon interaction in ultrathin ZrNCl nanosheets. The unprecedentedly giant heat flow generated from ZrNCl ultrathin nanosheets reached as high as 5.25 W/g with efficiency of 72%, which was dozens of times higher compared with that of traditional wide band gap semiconductors, such as nanocrystals of TiO_2 (0.26 W/g), ZnO (0.16 W/g), or SnO_2 (0.07 W/g), also recording the best value of UV photothermal effect among inorganic materials nowadays. The successfully realized giant UV photothermal effect in 2D nanomaterials represents a new effective energy conversion form from UV light. We anticipate that intense electron−phonon interaction in the quantum confinement system would be a powerful tool to achieve an efficient photothermal effect in inorganic solids.

MATERIALS AND METHODS

Materials. Zirconium powder (≥92.0%), ammonium chloride, and *n*-butyllithium (*n*-BuLi) (2.5 M in hexane) were all purchased from Sinopharm Chemical Reagent Co. Ltd. and used without further purification.

Synthesis of Bulk *β*-ZrNCl. *β*-ZrNCl powder was prepared in two steps: in the first step, *β*-ZrNCl with ZrO_2 impurity was synthesized through a high-temperature solid reaction, in which 5 mmol Zr and 5.5 mmol NH_4Cl were ground to mix homogeneously and then sealed into a 4 mL quartz-lined autoclave. The autoclave was heated at a heating rate of 3 °C/min to 650 °C and maintained for 3 h. The system was then allowed to cool to room temperature. The light green product was directly collected from the quartz lining without washing. In the second step, the obtained mixed product (ZrNCl and ZrO_2) was purified *via* the process reported previously.[33] A mixture of 300 mg of as-obtained product with 50 mg of NH_4Cl was vacuum-sealed in a quartz tube and horizontally placed in the furnace with a temperature gradient from 750 to 850 °C. The purified *β*-ZrNCl was transported into the high-temperature zone in 1 day. Then, the higher temperature zone (850 °C) was first cooled to 750 °C with a cooling rate of 2 °C/min, while the lower temperature zone was maintained at 750 °C. Afterward, these two temperature zones were cooled to room temperature with the same cooling rate at 2 °C/min.

Preparation of Precursor Li_xZrNCl. Li_xZrNCl precursor was prepared by a lithium intercalation process. The 20 mg of pure ZrNCl powder was dispersed in 2 mL of hexane with 0.5 mL of *n*-BuLi in a customized glass vacuum system. The reaction system was stirred and kept at 60 °C for 10 h. The obtained dark dispersion was filtered, washed with cyclohexane, and vacuum-dried at 60 °C for 30 min.

Exfoliation of Li_xZrNCl into ZrNCl Nanosheets. The as-obtained Li_xZrNCl was dispersed in 15 mL of distilled water and ethanol mixture (V_{H_2O}/V_{EtOH} = 2:1). The Li_xZrNCl-containing solution was bubbled with nitrogen to expel dissolved oxygen to avoid oxidation and then ultrasonicated for 3 h. The resulting suspension was centrifuged at 2500 rpm for 20 min to remove unexfoliated flakes, and the remaining supernatant was a high-quality dispersion of ZrNCl nanosheets.

Photo-DSC Measurement. In order to measure heat evolution accurately, the photo-DSC apparatus was set in an isothermal environment, which was kept at 25 °C while the source of photons was turned on and off. In this measurement, a 0.50 mg sample was spread out at the bottom of an open aluminum pan; meanwhile, an empty aluminum pan was used as a reference. UV light was emitted from a quartz light guide with a power of 200 mW/cm^2, which vertically irradiated the sample and the blank reference.

Conflict of Interest: The authors declare no competing financial interest.

Acknowledgment. This work was financially supported by the National Basic Research Program of China (2015CB932302), National Natural Science Foundation of China (Nos.21222101, U1432133, 11132009, 21331005, 11321503, J1030412), Chinese Academy of Science (XDB01010300), the Fok Ying-Tong Education Foundation, China (Grant No.141042), and the Fundamental Research Funds for the Central Universities (No. WK2060190027).

Supporting Information Available: Experimental materials and methods, characterizations, calculation details, and comparison experiments results. This material is available free of charge *via* the Internet at http://pubs.acs.org.

REFERENCES AND NOTES

1. Murdoch, M.; Waterhouse, G. I. N.; Nadeem, M. A.; Metson, J. B.; Keane, M. A.; Howe, R. F.; Llorca, J.; Idriss, H. The Effect of Gold Loading and Particle Size on Photocatalytic Hydrogen Production from Ethanol over Au/TiO_2 Nanoparticles. *Nat. Chem.* **2011**, *3*, 489–492.
2. Levskaya, A.; Weiner, O. D.; Lim, W. A.; Voigt, C. A. Spatiotemporal Control of Cell Signalling Using a Light-Switchable Protein Interaction. *Nature* **2009**, *461*, 997–1001.
3. Karoui, R.; Downey, G.; Blecker, C. Mid-Infrared Spectroscopy Coupled with Chemometrics: A Tool for the Analysis of Intact Food Systems and the Exploration of Their Molecular Structure−Quality Relationships: A Review. *Chem. Rev.* **2010**, *110*, 6144–6168.
4. Roy, N.; Sohn, Y.; Pradhan, D. Synergy of Low-Energy {101} and High-Energy {001} TiO_2 Crystal Facets for Enhanced Photocatalysis. *ACS Nano* **2013**, *7*, 2532–2540.
5. Timmerman, D.; Izeddin, I.; Stallinga, P.; Yassievich, I. N.; Gregorkiewicz, T. Space-Separated Quantum Cutting with Silicon Nanocrystals for Photovoltaic Applications. *Nat. Photonics* **2008**, *2*, 105–109.
6. Lu, Q.; Lu, Z.; Lu, Y.; Lv, L.; Ning, Y.; Yu, H.; Hou, Y.; Yin, Y. Photocatalytic Synthesis and Photovoltaic Application of $Ag\text{-}TiO_2$ Nanorod Composites. *Nano Lett.* **2013**, *13*, 5698–5702.

7. Feng, W.; Han, C.; Li, F. Upconversion-Nanophosphor-Based Functional Nanocomposites. *Adv. Mater.* **2013**, *25*, 5287–5303.
8. Kisch, H. Semiconductor Photocatalysis—Mechanistic and Synthetic Aspects. *Angew. Chem., Int. Ed.* **2013**, *52*, 812–847.
9. Xu, M.; Da, P.; Wu, H.; Zhao, D.; Zheng, G. Controlled Sn-Doping in TiO_2 Nanowire Photoanodes with Enhanced Photoelectrochemical Conversion. *Nano Lett.* **2012**, *12*, 1503–1508.
10. Tang, T.-T.; Zhang, Y.; Park, C.-H.; Geng, B.; Girit, C.; Hao, Z.; Martin, M. C.; Zettl, A.; Crommie, M. F.; Louie, S. G.; et al. Tunable Phonon−Exciton Fano System in Bilayer Graphene. *Nat. Nanotechnol.* **2010**, *5*, 32–36.
11. Bach, U.; Lupo, D.; Comte, P.; Moser, J. E.; Weissortel, F.; Salbeck, J.; Spreitzer, H.; Gratzel, M. Solid-State Dye-Sensitized Mesoporous TiO_2 Solar Cells with High Photon-to-Electron Conversion Efficiencies. *Nature* **1998**, *395*, 583–585.
12. Chen, L.; Zou, R.; Xia, W.; Liu, Z.; Shang, Y.; Zhu, J.; Wang, Y.; Lin, J.; Xia, D.; Cao, A. Electro- and Photodriven Phase Change Composites Based on Wax-Infiltrated Carbon Nanotube Sponges. *ACS Nano* **2012**, *6*, 10884.
13. Wang, Y.; Tang, B.; Zhang, S. Single-Walled Carbon Nanotube/Phase Change Material Composites: Sunlight-Driven, Reversible, Form-Stable Phase Transitions for Solar Thermal Energy Storage. *Adv. Funct. Mater.* **2013**, *23*, 4354.
14. Thirugnanasambandam, M.; Iniyan, S.; Goic, R. A Review of Solar Thermal Technologies. *Renewable Sustainable Energy Rev.* **2010**, *14*, 312–322.
15. Tielrooij, K. J.; Song, J. C. W.; Jensen, S. A.; Centeno, A.; Pesquera, A.; Zurutuza Elorza, A.; Bonn, M.; Levitov, L. S.; Koppens, F. H. L. Photoexcitation Cascade and Multiple Hot-Carrier Generation in Graphene. *Nat. Phys.* **2013**, *9*, 248–252.
16. Xu, M.; Liang, T.; Shi, M.; Chen, H. Graphene-like Two-Dimensional Materials. *Chem. Rev.* **2013**, *113*, 3766–3798.
17. Huang, X.; Zeng, Z.; Zhang, H. Metal Dichalcogenide Nanosheets: Preparation, Properties and Applications. *Chem. Soc. Rev.* **2013**, *42*, 1934–1946.
18. Butler, S. Z.; Hollen, S. M.; Cao, L.; Cui, Y.; Gupta, J. A.; Gutiérrez, H. R.; Heinz, T. F.; Hong, S. S.; Huang, J.; Ismach, A. F.; et al. Progress, Challenges, and Opportunities in Two-Dimensional Materials Beyond Graphene. *ACS Nano* **2013**, *7*, 2898–2926.
19. Sun, Y.; Gao, S.; Xie, Y. Atomically-Thick Two-Dimensional Crystals: Electronic Structure Regulation and Energy Device Construction. *Chem. Soc. Rev.* **2014**, *43*, 530–546.
20. Buhro, W. E.; Colvin, V. L. Semiconductor Nanocrystals: Shape Matters. *Nat. Mater.* **2003**, *2*, 138–139.
21. Chhowalla, M.; Shin, H. S.; Eda, G.; Li, L. J.; Loh, K. P.; Zhang, H. The Chemistry of Two-Dimensional Layered Transition Metal Dichalcogenide Nanosheets. *Nat. Chem.* **2013**, *5*, 263–275.
22. Sun, Y.; Lei, F.; Gao, S.; Pan, B.; Zhou, J.; Xie, Y. Atomically Thin Tin Dioxide Sheets for Efficient Catalytic Oxidation of Carbon Monoxide. *Angew. Chem., Int. Ed.* **2013**, *52*, 10569–10572.
23. Naguib, M.; Mashtalir, O.; Carle, J.; Presser, V.; Lu, J.; Hultman, L.; Gogotsi, Y.; Barsoum, M. W. Two-Dimensional Transition Metal Carbides. *ACS Nano* **2012**, *6*, 1322–1331.
24. Ye, J. T.; Inoue, S.; Kobayashi, K.; Kasahara, Y.; Yuan, H. T.; Shimotani, H.; Iwasa, Y. Liquid-Gated Interface Superconductivity on an Atomically Flat Film. *Nat. Mater.* **2010**, *9*, 125–128.
25. Hughes, A. E.; St. John, H.; Kountouros, P.; Schubert, H. Moisture Sensitive Degradation in TiO_2-Y_2O_3-ZrO_2. *J. Eur. Ceram. Soc.* **1995**, *15*, 1125–1134.
26. Lin, C.; Zhu, X.; Feng, J.; Wu, C.; Hu, S.; Peng, J.; Guo, Y.; Peng, L.; Zhao, J.; Huang, J.; et al. Hydrogen-Incorporated TiS_2 Ultrathin Nanosheets with Ultrahigh Conductivity for Stamp-Transferrable Electrodes. *J. Am. Chem. Soc.* **2013**, *135*, 5144–5151.
27. Staii, C.; Johnson, A. T.; Pinto, N. J. Quantitative Analysis of Scanning Conductance Microscopy. *Nano Lett.* **2004**, *4*, 859–862.
28. Asher, S. A. Ultraviolet Raman Spectrometry. In *Handbook of Vibrational Spectroscopy*; Chalmers, J. M., Griffiths, P. R., Eds.; John Wiley & Sons Ltd: Chichester, UK, 2002; p 3316.
29. Cros, A.; Cantarero, A.; Beltrán-Porter, D.; Oró-Solé, J.; Fuertes, A. Lattice Dynamics of Superconducting Zirconium and Hafnium Nitride Halides. *Phys. Rev. B* **2003**, *67*, 104502.
30. Gabor, N. M.; Song, J. C. W.; Ma, Q.; Nair, N. L.; Taychatanapat, T.; Watanabe, K.; Taniguchi, T.; Levitov, L. S.; Jarillo-Herrero, P. Hot Carrier-Assisted Intrinsic Photoresponse in Graphene. *Science* **2011**, *334*, 648–652.
31. Liu, X.; Zhou, K.; Wang, L.; Wang, B.; Li, Y. Oxygen Vacancy Clusters Promoting Reducibility and Activity of Ceria Nanorods. *J. Am. Chem. Soc.* **2009**, *131*, 3140–3141.
32. Guan, M.; Xiao, C.; Zhang, J.; Fan, S.; An, R.; Cheng, Q.; Xie, J.; Zhou, M.; Ye, B.; Xie, Y. Vacancy Associates Promoting Solar-Driven Photocatalytic Activity of Ultrathin Bismuth Oxychloride Nanosheets. *J. Am. Chem. Soc.* **2013**, *135*, 10411–10417.
33. Ohashi, M.; Yamanaka, S.; Sumihara, M.; Hattori, M. Novel Synthesis of the Layer Structured β-ZrNCl by the Direct Reactions of Zirconium Metal or Zirconium Hydride with Ammonium Chloride. *J. Solid State Chem.* **1988**, *75*, 99.